33RD CONGRESS
OF THE INTERNATIONAL COUNCIL
OF THE AERONAUTICAL SCIENCES
STOCKHOLM, SWEDEN, 4-9 SEPTEMBER, 2022

ICAS 2022 SWEDEN

DESIGN AND EXPERIMENTAL TESTING OF A DROOP NOSE MORPHING FOR ADVANCED REGIONAL AIRCRAFT

Alessandro De Gaspari[1], Vittorio Cavalieri[1] & Sergio Ricci[1]

[1]Politecnico di Milano, Via La Masa 34, 20156 Milano, Italy

Abstract

Morphing wing structures can improve the aircraft performances thanks to the possibility to adapt the wing shape throughout the mission. In this paper, a multi-level multi-disciplinary optimization procedure has been applied to the design of a morphing Droop Nose device, in the framework of Clean Sky 2 REG-IADP AIRGREEN 2 project. The procedure starts from the initial design requirements and achieves the design, manufacturing and testing of two experimental ground demonstrators for the assessment of the developed concept. The experimental tests enable the validation of the numerical results and demonstrate the effectiveness of the proposed morphing technology.

Keywords: morphing droop nose, compliant structures, multi-disciplinary optimization, 3D printing, experimental validation

1. Introduction

Morphing structures represent a promising technology for the design of more efficient aircraft. Thanks to the capability of continuously changing their shape in flight, morphing wings enable multi–point optimization of aircraft performances across the flight envelope. Different morphing concepts have been investigated over the years [1]. Among the others, the active camber morphing is a concept that can replace conventional flight control surfaces with innovative adaptive devices. Removing hinges and gaps can provide with many benefits, especially in terms of aerodynamic performances. The outcome is the potential reduction of fuel consumption and noise [2, 3]. In the category of high–lift morphing devices, the use of morphing droop nose, able to achieve high deflections, seems to be promising, and interesting technological solutions have been proposed in the literature. At the current state of the art, the most innovative solutions combine flexible skins and internal kinematics based on rigid components joined by mechanical hinges [4].

Morphing structures represent a challenge from the design viewpoint, due to two main reasons. On the one hand the design must take into account the strong interaction between the different disciplines involved in the functioning of the morphing devices [5]. On the other hand any design procedure has to deal with the so–called morphing paradox. The morphing structure must be stiff enough to withstand the aerodynamic loads and at the same time it must be flexible enough to allow for the morphing shape change [6]. The main concern is related to the design of an adaptive structure able to achieve shape changes while being insensitive to external load variations. This important requirement must be properly considered in the design procedure. Moreover, many other aspects must be taken into account to correctly assess the overall benefits of morphing concept: weight, complexity, actuation power, manufacturing technology, interaction of the device with the wing–box structure.

In the last 15 years the Department of Aerospace Science and Technology at Politecnico di Milano (Polimi) has joined many research programs on morphing [7, 8]. Different optimization tools have been developed over the years to deal with the different phases and requirements of the design of morphing devices, up to the realization of a complete multi–level and multi–disciplinary procedure for the design of active camber morphing devices [9]. This design procedure is based on dedicated optimization algorithms aiming at the synthesis of fully compliant structures able to transmit both forces and moments from the internal structure to the flexible skin. In this way the skin can be deformed to achieve optimal aerodynamic shapes and, at the same time, ensure the structural stiffness required to counteract any load condition. The design procedure starts from the design requirements in terms of aerodynamic performance augmentation, faces the challenge of designing the morphing structure, validates the numerical solutions through virtual models of increasing fidelity, up to the realization of real prototypes for the experimental assessment. This last point is particularly important. Indeed, only the manufacturing of prototypes and their experimental testing can show the actual performances of the technology, providing with essential information to increase the Technology Readiness Level (TRL) of the concept, which is fundamental for implementation on real aircraft.

This paper describes the design and experimental testing of a morphing Droop Nose ground demonstrator at different scales. The morphing droop nose is one of the morphing devices to be installed on an advanced regional aircraft in the framework of Clean Sky 2 REG-IADP AIRGREEN 2 (AG2) project. The paper summarizes the optimization procedure adopted for the design of the device up to the realization of a full-scale virtual demonstrator. Then, the paper describes the design, at different scales, of two ground demonstrators of the device, which are experimentally tested to assess the functionality of the device and to validate the design procedure.

1.1 Design Requirements

The main goal of the morphing droop nose is to delay the wing stall of the aircraft in high-lift conditions and, at the same time, preserve the Natural Laminar Flow (NLF) wing shape in cruise. For this reason, the skin must be flexible, to avoid any kind of step and gap, and it must be able to achieve very high deflections within its structural limits. A maximum curvature change of 20 1/m avoids normal strain due to bending above 1%. An internal compliant structure connected to a rotary electromechanical actuator through a kinematic chain is conceived to achieve the external shape change of the skin, according to performance requirements. These aerodynamic requirements prescribe a minimum increment of the aircraft lift coefficient in take-off and landing configurations of 2.5% and 1.8% respectively. The chordwise configuration of the device is defined by the front spar position, which is placed at the 16% of the local chord. The spanwise configuration covers all the wing inboard region and the outboard region from the nacelle up to the aileron.

2. Design and Verification Procedure

The design of morphing devices based on compliant structures is a challenging task, due to the presence of conflicting requirements, because a trade-off between flexibility and stiffness is needed [1]. To overcome these difficulties, dedicated design procedures must be adopted based on optimization techniques in a multi-disciplinary environment. The approach adopted in this work consisted of a multi-level and multi-disciplinary procedure, represented in Figure 1, composed by four main steps:

1. Definition of the optimal morphing shape using an in-house parametric optimization of the aerodynamic shape.
2. Application of a topology optimization to define a compliant structure able to deform itself to match the optimal shape coming from the previous step.
3. Application of a sizing optimization to refine the design and to apply the optimal topology solution to specific cases.
4. Realization of two experimental demonstrators for testing and verification: a half-scale 3D-printed demonstrator made of polyamide-based material and a full-scale demonstrator made of aeronautical materials.

The details of the first three steps applied to the design of the morphing droop nose are reported in the following subsections, while the two demonstrators, their design and the main results obtained after the validation tests are described in the last two sections of this paper. The two demonstrators have

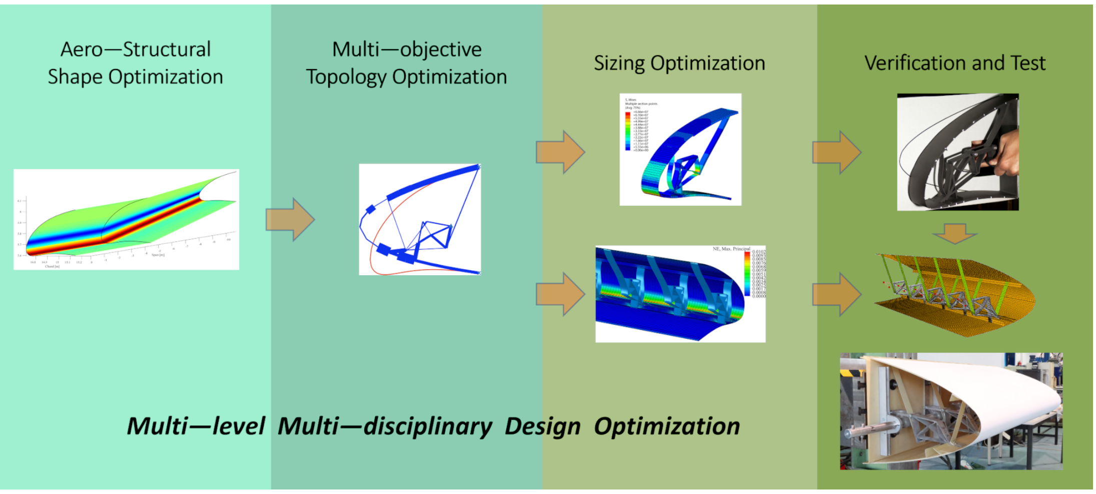

Figure 1 – Optimization procedure for the design and verification of the morphing droop nose.

been designed and tested to validate the proposed concept of morphing droop nose in the framework of Clean Sky 2 AG2 activities. The first one is a 3D printed half-scale model for the initial validation of the concept. The second one is a full–scale model to assess the functionality of the solution at the actual scale and using aeronautical materials. Starting from the same topology solution, the local sizing optimization, corresponding to the design step number 3, has been performed to apply the common topology to the design of the two experimental prototypes.

2.1 Aero-Structural Shape Optimization

In the first step, a suitable parametrization technique, namely the Class/Shape function Transformation (CST) [10], extended to morphing wings [9], has been adopted to describe the morphing wing geometry by a small set of design variables. Starting from the shape change, the algorithm can also reproduce the structural behaviour of the skin, computing the associated axial and bending strains. An aerodynamic shape optimization based on RANS computations has been used to define a morphing shape that satisfies the skin structural feasibility and that is characterized by the optimal aerodynamic performances demanded by the design requirements. In particular, the morphing droop nose is able to increase the stall angle of 2.5 deg in the take–off configuration, while it increases the stall angle of 5 deg in landing configuration. The aerodynamic benefits have been evaluated at aircraft level through high–fidelity CFD simulations. The corresponding maximum lift coefficients are higher than the design requirements, as shown in Figure 2, together with a wing view of the reference aircraft.

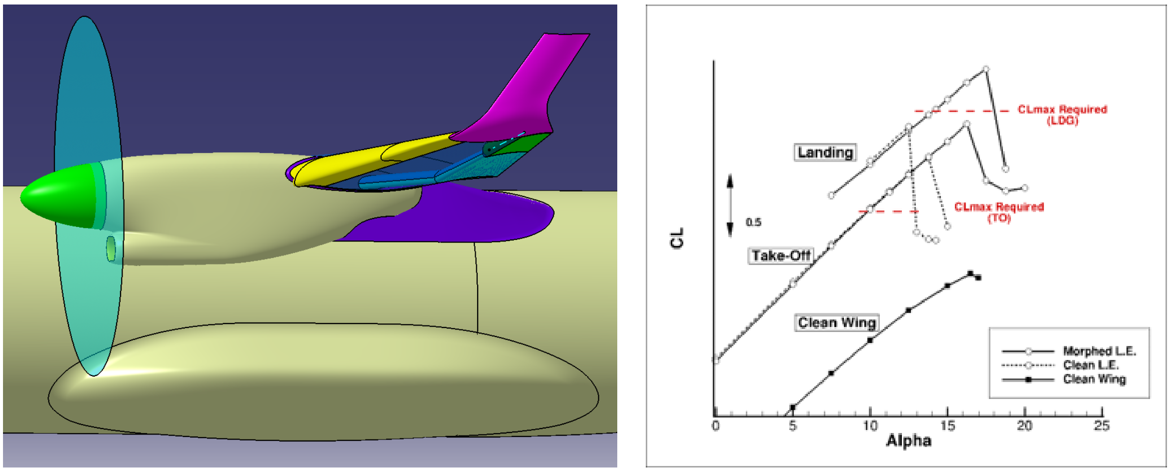

Figure 2 – Reference aircraft equipped with morphing droop nose and effect of the morphing droop nose on the performance in take–off and landing configurations.

The equivalent deflection of the device is constant in the inboard region with a value of 16 deg, and it decreases in the outboard region from 16 deg to 10 deg.

2.2 Topology Optimization

In the second step, the optimal morphing shape has been used as target shape for the design of the compliant structure based on the distributed compliance concept, where only flexible elements are used instead of rigid mechanical components [11]. The design tool consists of a topology optimization based on a Load Path Representation which is coupled with nonlinear analyses, performed on low-fidelity finite element models (FEM), and a dedicated multi-objective genetic algorithm. Two main objective functions have been considered to meet both kinematic and structural requirements: the minimization of the Strain Energy to preserve the NLF wing shape when the mechanism is not actuated, and the minimization of the Least Square Error (LSE) between the target shape and the skin deformed shape achieved when the mechanism is actuated. Since the multi-objective genetic algorithm finds multiple optimal solutions, at the end of the process one topology solution has been selected directly from the Pareto Front, taking into account also the manufacturing requirements, which were not included in the formulation of the optimization problem. The selected topology solution is illustrated in Figure 3, which also depicts the optimal target shape.

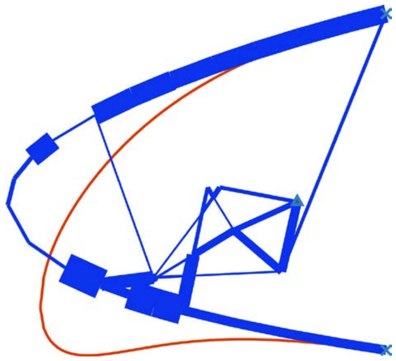

Figure 3 – Topology solution selected from the Pareto Front of the multi-objective genetic algorithm.

2.3 Sizing Optimization

The structural solution obtained from the global optimization can be refined with a local optimization, based on Sequential Quadratic Programming (SQP) algorithm. The adopted tool is a sizing optimization performed to find the thickness distribution of the mechanism and the skin able to improve the quality of the deformed shape, under structural constraints. In general, it is appropriate to perform local optimization after global optimization to enhance the global optimum solution. In addition, the adopted sizing optimization is capable of applying design modifications to the topology solution of the second step. The modifications can concern material change and geometric change, including scale change. Initially, the described tool has been applied to the design of a full–scale virtual demonstrator of the entire device [12]. It consists of 20 equally spaced aluminium ribs connected to a glass-fibre reinforced polymer skin in correspondence of four stringers. The size of the ribs is slightly different due to the tapering of the wing. Therefore, starting from the topology solution, the root rib and the tip rib have been refined to locally match the external target shape. Then, the optimal variables have been interpolated in the spanwise direction to define the complete structure of the device. Different FEM verifications have been performed to validate the solution, including structural feasibility assessment, evaluation of the quality of the 3D morphing shape, study of the interaction between the device and the wing-box. The results showed that the design requirements were satisfied. The FEM model of the virtual demonstrator is represented in Figure 4 in the morphing configuration.
After this phase, the same optimization tool is applied to realize two experimental demonstrators, as described in the following section.

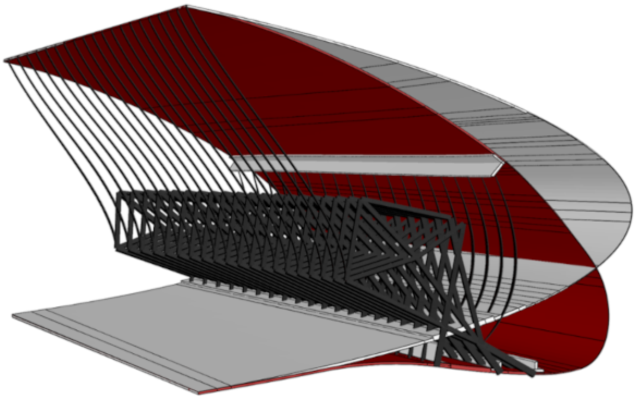

Figure 4 – Three-dimensional morphing configuration virtual demonstrator.

3. Half-scale Prototype

The design of this prototype is based on the use of a dedicated optimization procedure able to deal with material and geometric changes. Thanks to this procedure, it is possible to scale down the full-scale topology of the second step by re-optimizing the size and shape variables according to the scaled model requirements. The main goal is to scale the topology solution from the structural perspective by acting on the size variables and on the shapes of all manufacturing details, such as fillets and connections, according to the new geometric scale and to the adopted material. The starting point for the design is the same initial topology solution found for the full-scale device. However, the same materials chosen at the full-scale level cannot be adopted at the reduced scale due to the augmented curvature changes required at the half-scale. Instead, less stiff materials are needed for this application. Therefore, the geometric scale change is introduced in combination with the adoption of a polyamide-based material. The choice of this material is based on previous experience at Polimi [8], and 3D printing technology is used to manufacture the scaled model. The adopted technique is the selective laser sintering (SLS) in combination with a fine powder that is based on polyamide, whose mechanical characteristics are reported in Table 1.

Table 1 – Mechanical parameters of the polyamide-based material.

Parameter	Value
Flexural Modulus	1.82 GPa
Poisson’s ratio	0.35
Flexural Strength	67.6 MPa

This type of material and the related manufacturing technique are specifically selected to realize components that are flexible but guarantee the required stiffness. Moreover, the material and the technique perfectly satisfy the objective of realizing morphing devices in a single piece. Moreover, it is also possible to directly manufacture the actuation kinematic chain together with the device, without the need to assembly them. To ease the manufacturing process, the same material is used for the skin, the internal structure, and the kinematic chain.

3.1 Sizing Optimization

The airfoil geometry, the internal structure, the rib pitch and the rib thickness are scaled down by a factor 2. The initial half-scale solution and the full-scale one are represented in Figure 5.

The polyamide-based material, whose parameters are reported in Table 1, is selected for the compliant rib and the skin. Regarding the load conditions to consider in the design process, it must be noted that the half-scale model is not conceived for wind tunnel tests but for an experimental functionality test. However, the aerodynamic loads are included in the optimization procedure because the application of aerodynamic loads helps to obtain a flexible device that can achieve a deterministic external shape, which is as much as possible independent of the external loads. Therefore, the aerodynamic

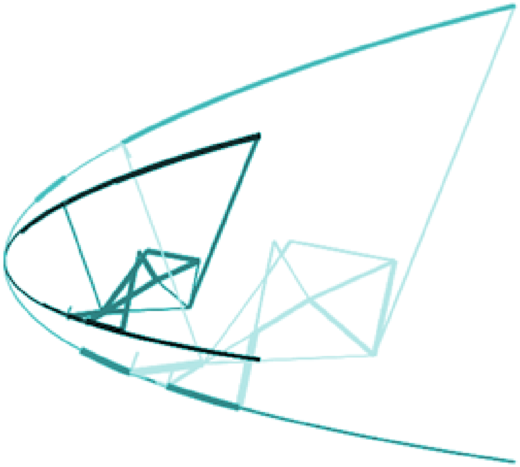

Figure 5 – Full-scale and half-scale models.

loads are applied on both the undeformed and the deployed conditions. The aerodynamic conditions selected for the structural requirement constraint are Mach=0.148 and $\alpha = 0°$. The objective function that corresponds to the kinematic requirement is computed considering the pressure distribution of the landing condition after scaling the dynamic pressure. The design variables of the optimization analysis are the size variables of both the rib and the skin, and they are bounded between 1 mm and 5 mm. The position of the internal points of the rib is left fixed. The sizing optimization is run to minimize the LSE, and it converges to a feasible optimal solution with LSE=2.6 mm and a maximum stress of 66.6 MPa. The comparison between the optimal deformed shape and the target shapes is presented in Figure 6. The deformed shape is computed with and without the aerodynamic loads, and the difference between them is negligible. Therefore, the designed prototype is able to act as a high-lift control surface, because the skin deformation is essentially indifferent to the presence of the external aerodynamic loads. As a consequence, the structural shape optimization described in the following can be performed without applying the aerodynamic loads, reproducing the experimental test conditions.

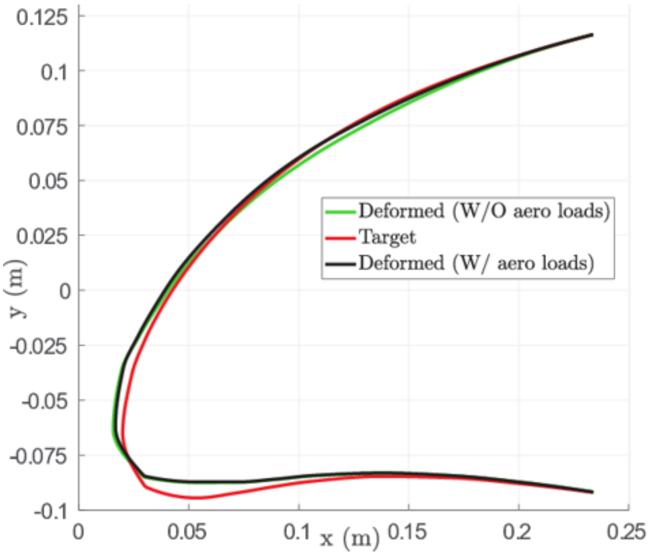

Figure 6 – Half-scale optimum solution obtained from sizing optimization: comparison between deformed and target shapes.

3.2 Structural Shape Optimization

Starting from the solution obtained by the sizing optimization, a complete Computer Aided Design (CAD) model of the half-scale prototype has been realized. Particular attention has been devoted to assign proper dimensions to the fillets inside the structure and to draw gradual transitions along the skin to avoid abrupt thickness changes. The CAD model has been imported into Abaqus, and it was finely meshed using 10-node quadratic tetrahedron elements for both the internal structure and the skin. The results of the static analysis demonstrated that the stress level increases due to local concentrations that the previous medium-fidelity model could not catch, up to a maximum value of 112 MPa inside the structure. Therefore, the shape optimization can be used to spread the stress, with the aim of reducing the peak values in two critical regions. The former is inside the structure, the latter is the bottom part of the skin where the maximum curvature variation is achieved during the deformation. The shape optimization process introduces shape changes around the critical regions to reduce the stress peaks. The results are reported in Figure 7.

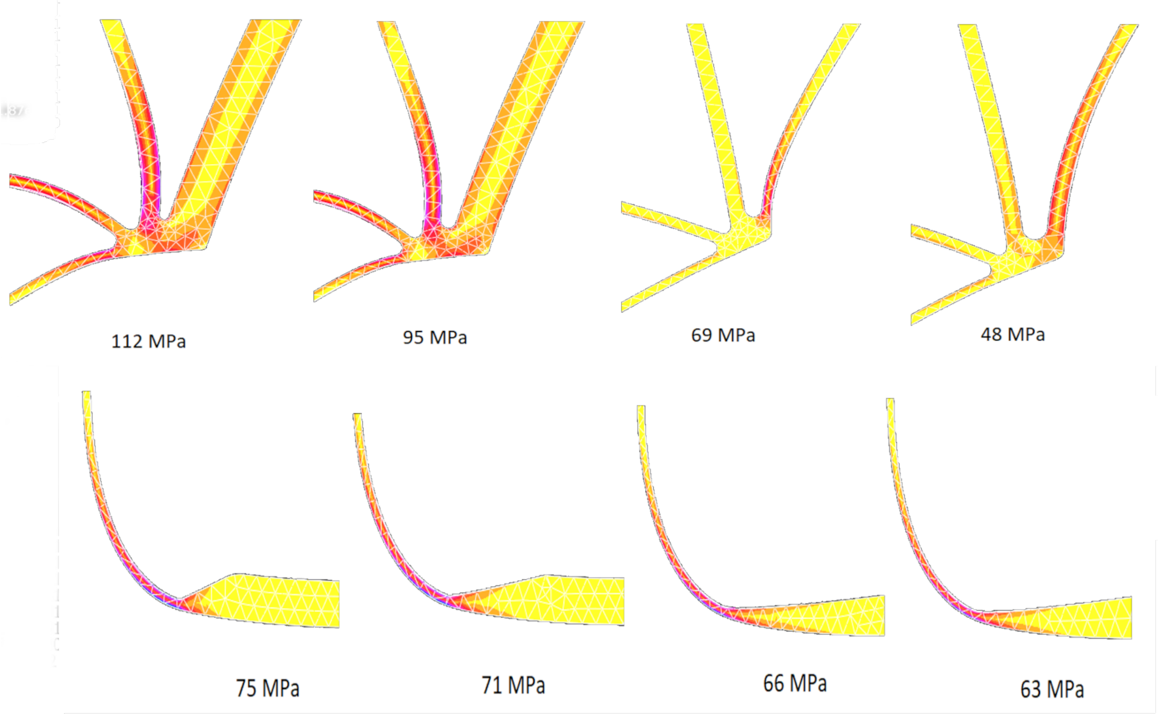

Figure 7 – Solution improvement for the most critical regions of the compliant rib (top) and the skin (bottom) during the structural shape optimization.

After the structural shape optimization, the shape quality of the optimal solution has been assessed, showing that the new result is substantially unchanged with respect to the optimal solution of the previous step. The final value of LSE is 2.7 mm, which is the same as the value that was obtained after sizing optimization. After the optimization process, the maximum stress in the structure decreased to 63 MPa; hence, the stress constraint is satisfied and the structural feasibility is assured.

3.3 Experimental Validation

Once the design of the half-scale prototype has been finalized and the detailed structural model has been obtained, the demonstrator has been manufactured and tested to validate the numerical solution and to study the overall behaviour of the adaptive droop nose from the experimental perspective.

The device corresponding to the optimal solution obtained with the shape optimization has been produced via a 3D printing technology, together with the kinematic chain conceived to actuate the compliant structure. The kinematic chain consists of a shaft, a cam and two rods. The sizes of these mechanical components have been designed by taking into account their internal forces. Moreover, a very thick block has been added in place of the front spar to ground the structure. The complete CAD model is shown in Figure 8 left, and it has been used as input for the SLS process, whose result is shown in Figure 8 center, which represents the manufactured prototype during the test.

The realized droop nose can be actuated by rotating the shaft up to reach the maximum design deflection of 70 deg. The shaft is equipped with two handles that achieve the horizontal position when the shaft is rotated 70 deg.

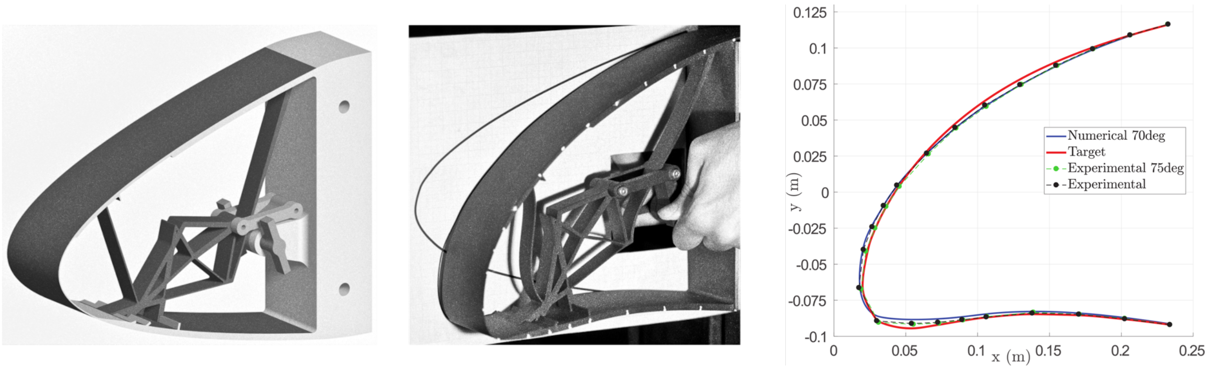

Figure 8 – Half-scale morphing droop nose prototype. CAD model (left), experimental test (center), comparison between numerical and experimental results (right).

The experimental tests are performed in the Polimi's laboratory for structural tests. No external loads are applied to the skin surface, and the corresponding numerical deformed shapes are used for validation. Two experimental verification approaches are considered. The former is a qualitative comparison between the deformed shape achieved by the deployed prototype and the optimal numerical shape obtained at the end of the optimization procedure. The latter involves the computation of the experimental LSE. In the first case, the experimental test is simply carried out by overlapping the deformed prototype with the numerical deformation printed on a paper. The comparison, which is depicted in Figure 8 right, shows satisfactory proximity between the two shapes. Moreover, the numerical and the experimental shapes are compared to the target shape. It can be seen that the quality of the prototype is better than the numerical one and it approaches the target shape. In the second case, the identification of the experimental deformation is performed by a simple photogrammetry technique that is based on a camera to recognize specific markers on the model. The device is equipped with 22 markers along the skin, which have been placed at the same arc-length positions of the points that are used to compute the numerical LSE. Some pictures of the deformed model were captured. Then, the pictures were digitally recognized, and the marker positions were used to reconstruct the experimental deformation. The identified curve is used to compute the experimental LSE. The comparison between the experimental curve, the target curve and the result of the numerical analysis are reported in Figure 9. The experimental curve is between the numerical and the target curves, hence the shape quality of the prototype appears better than the numerical one. The experimental LSE is 2.3 mm and it is comparable with the numerical LSE. Therefore, this quantitative validation shows a satisfactory numerical-experimental correlation. Successively, the shaft rotation was increased up to 75 deg to test the prototype behaviour beyond the target deflection. The corresponding curve is also reported in Figure 9, and it shows that the deflection further increases, deforming the upper part of the skin downwards. Finally, the device has been completely unloaded up to 0 deg rotation of the shape to show that the prototype matches again the undeformed shape. This confirms the elastic behaviour of the prototype that did not exceed the stress limit of the material. These outcomes prove the effectiveness of the proposed procedure to achieve a feasible solution. Moreover, the functionality of the designed device is as expected by numerical simulation.

4. Full-scale Prototype

The previous section demonstrated the possibility to scale down the morphing droop nose obtaining a device working in accordance to the requirements. However, the design of the half-scale device required to use a polyamide-based material. Therefore, a scaled model of a morphing device can be used only to reproduce the target shape corresponding to specific aerodynamic performances, but not to validate the structural and mechanical concept, which must be tested at full-scale level.

As a consequence, a full-scale version of the prototype, made of typical aeronautical materials, has been conceived, representing a portion, with span equal to 1.3m, of the complete full-scale device.

Starting from the same topology solution, many details of the morphing structure have been finalized, depending on the choice of materials and manufacturing technologies here adopted. The design

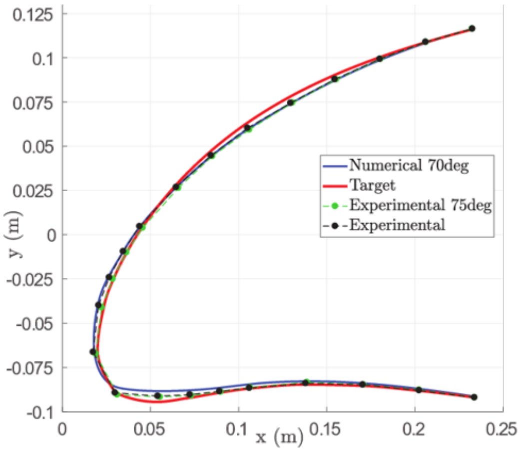

Figure 9 – Half-scale prototype: comparison between experimental and numerical deformed shapes.

process has been conducted through a series of iterations among the selected technological solutions and their numerical assessment in terms of achieved deformed shape and maximum level of stress inside the structure. Two main issues have been solved: the choice of the materials and how to realize the connections between the different parts of the device.

4.1 Design Optimization

The starting point for the optimum design of the full-scale prototype is the topology solution previously defined. As already said, the available optimization tools can be used to improve the solution by refining it according to the specific features of the device. The main weakness of the adopted topology solution is related to the high strain levels in the compliant ribs. Therefore, an alternative to the use of aluminium alloy is searched in this design phase. In particular, the highest strains in the internal structure concern the longest paths, which connect the central body of the rib to the upper skin. Therefore, hybrid-material internal ribs are conceived. The central body of the rib is left in aluminium, whereas the longest paths of the rib can be made of a composite material. Glass-fibre and carbon-fibre composite materials are evaluated with the aim of exploiting their high allowable strains, which can guarantee to obtain the target shape while satisfying the material limits.

The design of the prototype is based on a multi-objective sizing optimization, whose variables are the in-plane thicknesses of the rib and thickness distribution of the skin. As previously done, both kinematic and structural requirements are considered in the optimization analysis. In particular, the shape quality requirement in the morphing configuration must be satisfied, both with the aerodynamic loads in landing configuration and also without them. Moreover, the undeformed shape must withstand the aerodynamic loads. Finally, the structural feasibility of the solution must be ensured in all the considered conditions, namely the strains in the structures must be limited. The multi-objective optimization, minimizing the objective related to the above-mentioned requirements, has been performed twice, to evaluate both the glass-fibre and the carbon-fibre material. The Pareto Fronts of the two cases have been evaluated to establish the best trade-off between the various requirements and a solution characterized by the use of glass-fibre material has been selected. The deformed shape corresponding to the optimal structural solution is reported in Figure 10 compared with the target shape. The LSE value is 2.2 mm. The maximum principal strain in the glass-fibre is 2%.

4.2 Numerical Results

Starting from this refined solution, a high-fidelity FEM model of the full-span demonstrator has been realized to evaluate the three-dimensional shape quality and to perform the structural assessment. The model is made of five equally spaced ribs, the skin, and four stringers in correspondence of the connection between ribs and skin. The span of the device is 1.3 m and the wing geometry is slightly tapered. The ribs are perpendicular to the spar. The rib width is 40 mm and the rib spacing is 260 mm. Figure 11 represents the complete 3D FEM model.

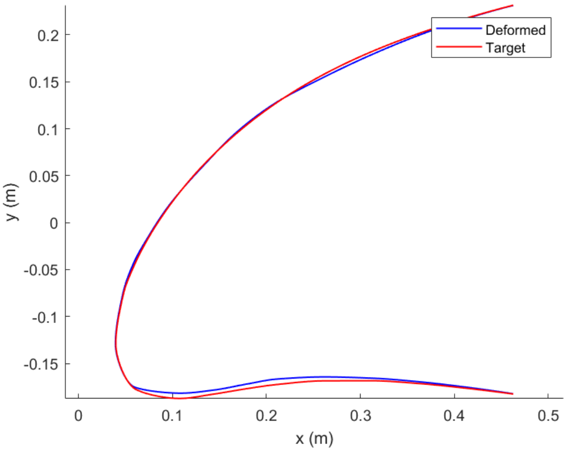

Figure 10 – Full-scale prototype: optimal solution deformed shape and target shape.

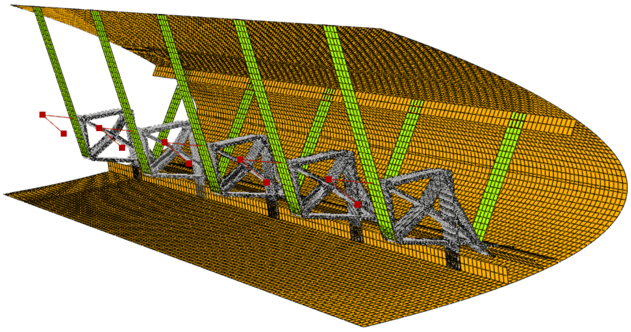

Figure 11 – 3D FEM model of the full-scale prototype.

The five ribs share the same thickness distribution found in the previous analysis, while their geometry is slightly different, according to the local dimensions of the wing. The effect of tapering is not so important hence the optimal sizing variables can be applied to all the ribs. The skin is divided in sectors extended along the span, based on the arc-length along the airfoil, and the optimal thickness distribution is applied.

Regarding the finite element modelling, the ribs are modelled using solid elements, while skin and stringers are modelled with shell elements. To reproduce the connection of the ribs to the skin in correspondence of the stringers, the shell elements of the stringers are tied to the solid elements of the ribs to prevent relative motion between them at the interface of the connection. The same constraints are used to connect the ribs longest paths to the stringers and to the central body of the ribs. The actuation mechanism used to achieve the morphing shape of the device is a kinematic chain made of shaft, cams and rods, properly designed to impose a displacement on all the ribs. The kinematic chain is modelled using rigid elements and the actuation is imposed by applying the rotation at the discrete points placed at the intersection between the shaft axis and the ribs planes.

Concerning the selection of the materials, S glass-fibre material is preferred to type E for its better mechanical properties, especially in terms of elongation at failure. The main features of the selected material are reported in Table 2.

All the optimum thickness values of the parts realized in glass-fibre material have been approximated in the model as integer multiples of the cured ply thickness, whose nominal value is 0.271 mm. The material selected for the central body of the ribs is the high resistance 7075 aluminium alloy. The estimated mass per unit length of the compliant structure (ribs and skin) is 9 kg/m.

The behaviour of the actuated model is simulated performing nonlinear FEM analyses. The behaviour of the complete demonstrator shows no substantial differences in terms of shape quality with respect to the single-rib model. The 3D morphing deformation is in good agreement with the target shape, as depicted in Figure 12. It can be seen that the deformed shape changes negligibly when applying or

Table 2 – Material properties of EE302S ER450 38%.

Parameter	Value
0° Tensile modulus	28.4 GPa
90° Tensile modulus	27.2 GPa
Poisson's ratio	0.16
In Plane Shear modulus	3.98 GPa
0° Tensile strength	687 MPa
0° Compressive strength	540 MPa
90° Tensile strength	580 MPa
90° Compressive strength	505 MPa
In Plane Shear strength	97.5 MPa
Elongation at failure	3.05%
Cured Ply Thickness	0.271 mm

not the aerodynamic pressure loads, confirming the validity of the adopted multi-objective approach to design a device stiff enough to withstand the external loads but able to change its shape realizing the morphing configuration. The deformed shapes correspond to a 80 deg rotation of the shaft, which can be obtained with an estimated actuation torque of 528 Nm or 576 Nm, respectively without and with external load applied.

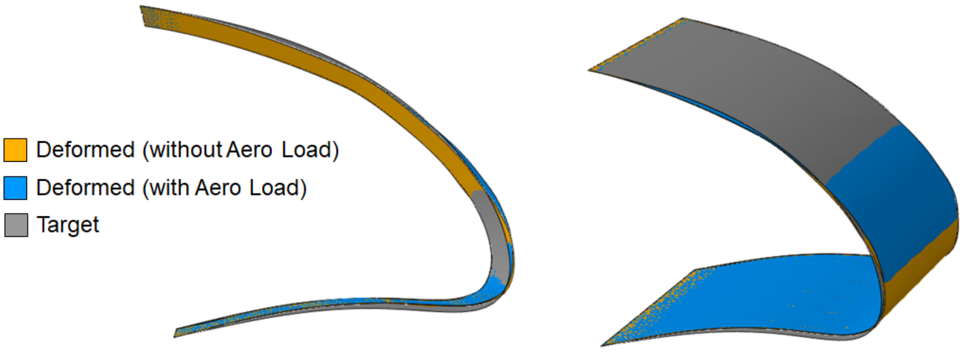

Figure 12 – Full-scale prototype: comparison between morphing deformed shapes (with and without aerodynamic load) and target shape.

Regarding the structural assessment, Tsai-Hill criterion is used for the composite material parts. The failure index in the skin is reported in Figure 13. Its maximum value is 0.79. Maximum Von Mises stress in the aluminium ribs is not critical.

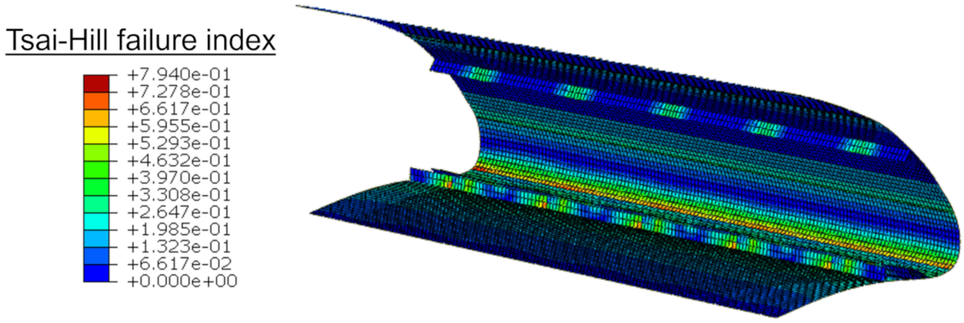

Figure 13 – Full-scale prototype: Tsai-Hill failure index in the skin.

4.3 Manufacturing

In parallel with the high-fidelity FEM model, the corresponding CAD model has been generated and gradually updated to find an engineering solution very easy to build and to assemble. The CAD model of the complete device is represented in Figure 14,

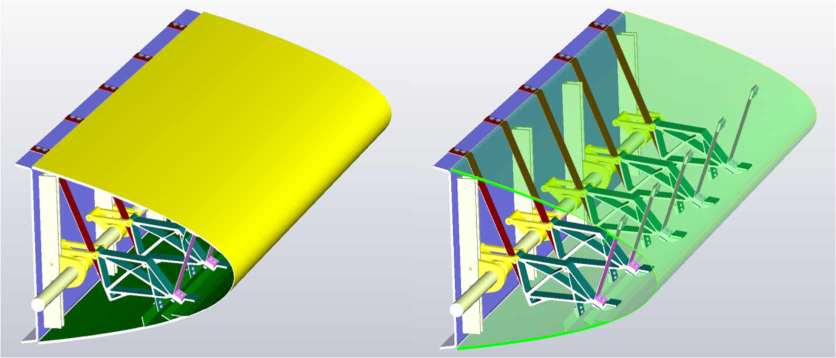

Figure 14 – CAD model of the full-scale prototype.

In this solution, four stringers are embedded into the skin to increase the spanwise stiffness, minimizing the anticlastic deformations, and to introduce the physical connections between the skin and the compliant ribs. In the stacking phase of the skin manufacturing, the laminae have been properly cut to realize a gradual transition between the adjacent regions characterized by different thicknesses. In the case of the half-scale model, shape optimization was needed to reduce stress concentrations in the skin. Here, the described operation has been performed to achieve a more smooth deformation of the external surface. The skin is constrained to a C-shape beam representing the spar of the wing-box to which the droop nose device should attach. It is also realized in glass-fibre, and it is stiffened with honeycomb panels.

The compliant ribs have been subjected to some modifications with respect to the numerical solution in order to ease the manufacturing process. In particular, the topology has been slightly simplified both to remove unnecessary details and to simplify the connection to the other parts. Water jet cutting technology has been then used to manufacture the central body of the ribs, and also cams and rods of the kinematic chain.

Finally, bolted joints ares selected to connect the ribs and the stringers and to assemble the rib pieces. Moreover, four supports are designed to connect the kinematic chain to the spar, to sustain the reaction loads coming from the actuated device.

After the manufacturing of all the components, the complete prototype is assembled, as depicted in Figure 15.

4.4 Experimental Testing

The experimental testing of the full-scale prototype has been a functionality test to validate the structural feasibility and to evaluate the external shape in the morphing configuration to be compared with the optimal target shape and the numerical solution.

The identification of the external shape of the device is performed by 3D Digital Image Correlation (DIC) photogrammetry. The selected technology has the capability to provide the identification of full-field displacements and strains. Instrumentation and software for the tests have been provided by SIEMENS. The employed instrumentation consists of two high-resolution cameras and a software able to perform the identification through the correlation of a pattern painted on the surface of the device. The test for the shape identification has been repeated twice, adopting two different configurations of the cameras because the size of the droop nose device and the deflection of interest prevented to film the entire deflection with the same fixed configuration. The first configuration focused on a bottom view of the device, whereas the second configuration focused on a top view. The two sets of results have been merged in the post-processing phase to obtain the complete shape of the device.

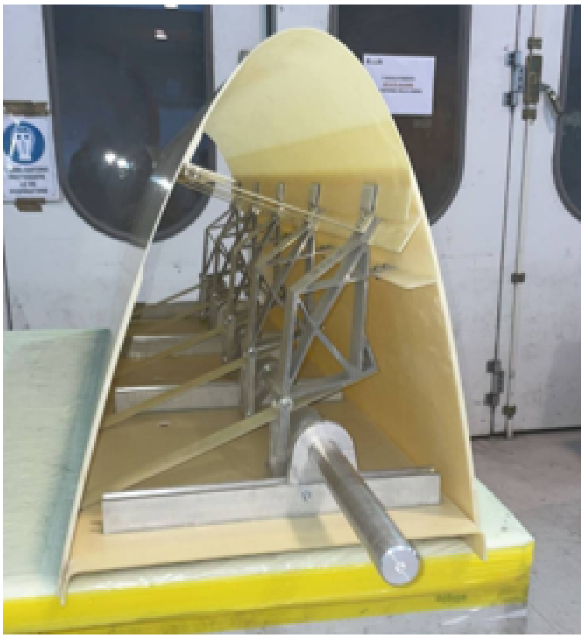

Figure 15 – Full-scale assembled prototype.

Some strain gauges have been installed on the device to measure forces and torque. The strain gauges installed on the shaft are used to measure the actuation torque applied to the shaft. The strain gauges installed on all the rods of the kinematic chain are used to measure the axial forces in the rods.

The experimental test is performed by using an electrodynamic rotating actuator to apply a torque to the shaft to obtain a certain angular position. Steps of 5 deg or 10 deg are successively performed up to a maximum rotation of 70 deg, which corresponds to an equivalent rotation of the device equal to 13.6 deg.

Figure 16 compares the undeformed shape of the device with the deformed shapes obtained at 40 deg, 60 deg, and 70 deg of shaft rotation. Figure 17 shows the detailed views of the root and the tip sections for the 70 deg morphing shape. Different loading and unloading cycles are performed to verify the elastic behaviour of the device, which always comes back to the undeformed configuration.

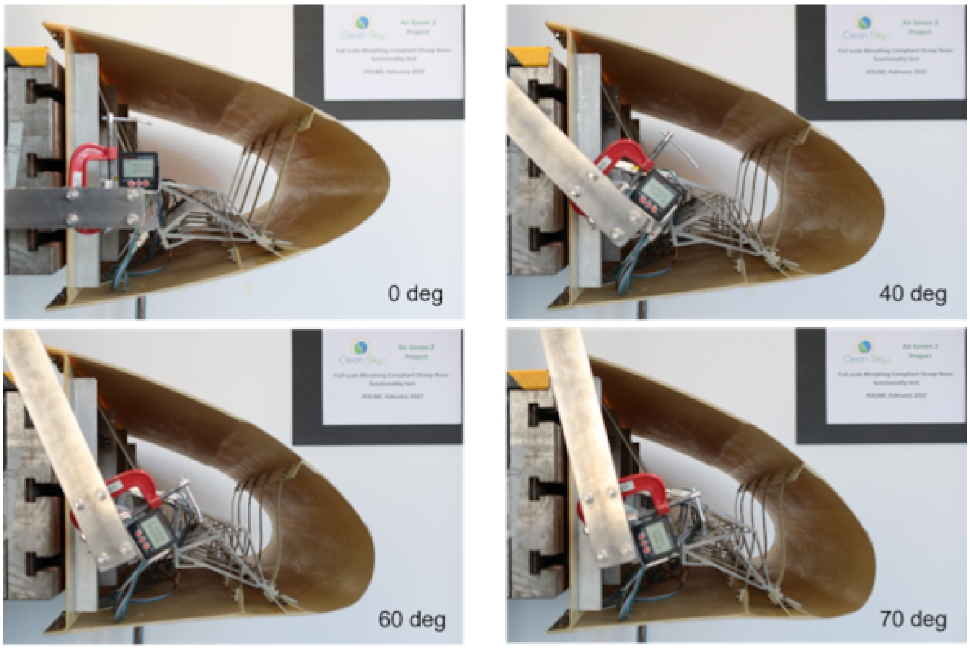

Figure 16 – Full-scale prototype: undeformed shape and deformed shapes

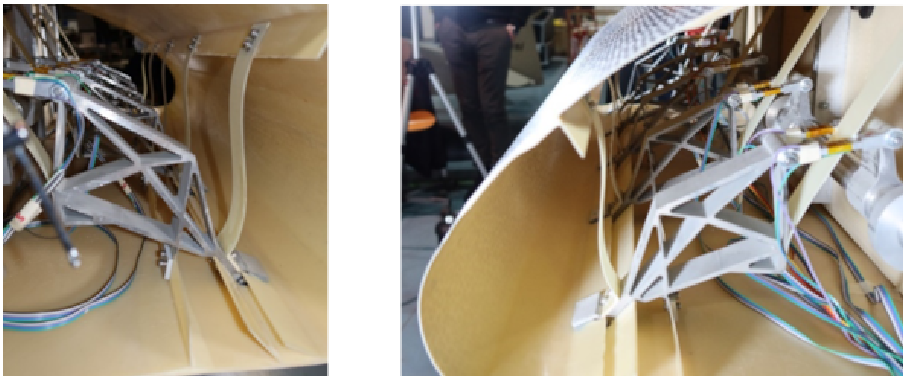

Figure 17 – Full-scale prototype: detailed view of root (left) and tip (right) sections of the device at 70 deg of shaft rotation.

Moreover, the undeformed configuration is loaded with vertical forces to test the ability of the device to bear several multiple of its own weight without appreciable deformation, confirming that the structural requirement is satisfied.

In the post-processing phase of the experimental test, the 3D shapes of the upper skin and the lower skin acquired by DIC are merged together by using the common data point locations from the undeformed model. This identified shape at 70 deg is compared with the corresponding deformed shape obtained by the numerical simulation, as illustrated in Figure 18. The comparison shows very nice quality of the experimental deformed shape and good accordance with what expected numerically, thus validating the structural design of the device. The 2D comparison in a section close to the root is also reported.

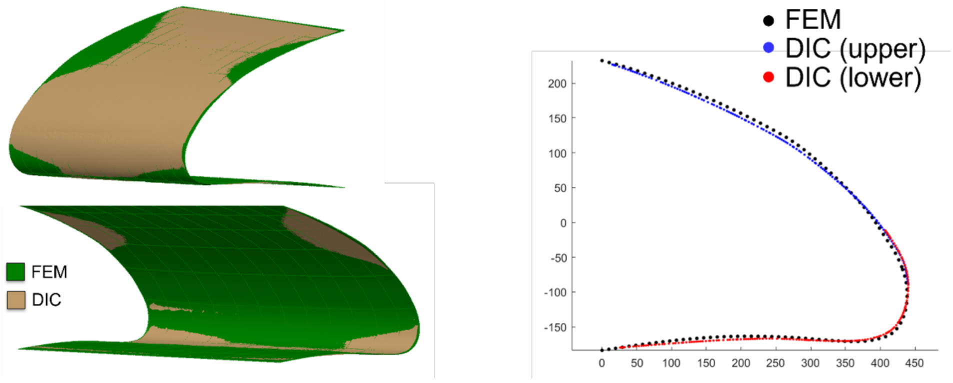

Figure 18 – Full-scale prototype: comparison of deformed shapes between DIC and FEM at 70 deg of shaft rotation.

Moreover, the maximum principal strains estimated by DIC are compared with FEM results. The comparison shows similar results in terms of contour, but the experimental strain values are greater than expected. This may be due to the use of only 2 cameras that could not guarantee accurate measure of full-field strains of the droop nose device.

Finally, the measured torque needed for the actuation of the morphing device is shown in Figure 19. The experimental torque here reported is estimated based on the axial forces measured in the rods. Instead, the torque values read at the shaft are affected by the friction in the shaft supports and are not useful for energetic considerations. The observed friction will be removed in future tests with the adoption of bearings. The comparison of the experimental torque with the numerical result is under investigation to conclude the numerical-experimental correlation.

5. Discussion

The optimization procedure described in this paper deals with the different phases of the design of a morphing droop nose. At the beginning, the device performances are mainly concerned, but

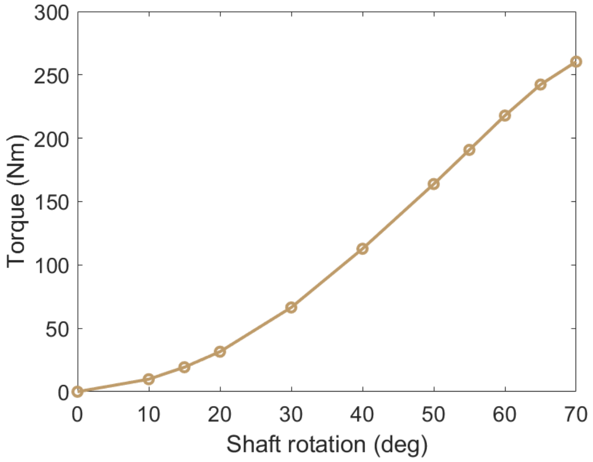

Figure 19 – Actuation torque for the full-scale prototype

the structural feasibility of the skin is already taken into account. Then, the main focus becomes the design of the compliant structure, starting from a topology solution that is gradually refined, by means of sizing and structural shape optimization, with the aim of improving the morphing behaviour but at the same time assuring the feasibility limiting the stresses inside the structure.

The design of two prototypes has shown the difficulties experienced when passing from the numerical solution to the fabrication of the device. Indeed, the choice of the materials, the related manufacturing techniques, the assembly issues, the structural feasibility must be properly evaluated to not compromise the expected performances of the optimal numerical solution. Therefore, the manufacturing and testing phases are fundamental to achieve a comprehensive view of the potentialities as well as the complexity related to the proposed morphing concept.

Regarding the experimental testing, it has been shown that reduced-scale prototyping involves specific issues that must be solved by dedicated design solutions, depending on the specific scale and requirements. Reduced-scale experimentation, if properly conducted, can provide with useful information about the behaviour of the device. However, it is not sufficient to completely evaluate the morphing concept. Indeed, full-scale experimentation is fundamental to validate the structural and mechanical concept, which must be tested at full-scale level. This concerns the assessment of the functionality but also the material selection, which must be suitable for the application of morphing devices on real aircraft.

Besides the structural feasibility assessment, the evaluation of the shape quality in the morphing configuration represents the primary information related to the performances of the device. Photogrammetry has proven to be a valid technique for the identification of the external shape. As an alternative, the adoption of fibre optics is intended as future work, also to investigate the possibility of real-time acquisition of the morphing shape.

6. Conclusions

This paper has shown the application of a multi-level multi-disciplinary procedure for the design of a morphing droop nose. The experimental activities carried out have shown the working principle and the functionality, both of a small reduced-scale device and at the full-scale level, demonstrating the effectiveness of the proposed morphing solution. In particular, the first application has demonstrated the possibility of adapting the full-scale topology to the geometry of a scaled model. Moreover, the manufacturing and testing of the designed prototype have validated the procedure and assessed the functional aspects of the proposed morphing strategy. The second application has been more complex, dealing with the prototype at real scale and using aeronautical materials. Even though the span dimension of the prototype is smaller than that of the device of the regional aircraft, the scale is the same and also the wing tapering is reproduced, hence the prototype should describe well the expected behaviour of the real device. The experimental testing has confirmed the functionality assessment of the morphing droop nose and has provided with important information about the issues related to the proposed concept. New experimental activities have been planned to overcome the encountered issues and also further numerical simulations will be performed to close the loop of the design procedure by computationally validating the aerodynamic performances associated to the experimental shape. Starting from the acquired experience, new research activities can further increase the TRL of the proposed morphing concept up to the realization of flight demonstrators to test the devices in real operating conditions.

7. Contact Author Email Address

mailto: alessandro.degaspari@polimi.it

8. Acknowledgements

The AirGreen2 Project has received funding from the Clean Sky 2 Joint Undertaking, under the European's Union Horizon 2020 research and innovation Programme, under grant agreement No. 807089. The authors would like to thank Davide Mastrodicasa, Emilio Di Lorenzo and Giancarlo Kosova from SIEMENS for their support during the 3D shape measurements through DIC technology.

9. Copyright Statement

References

[1] Barbarino, S., Bilgen, O., Ajaj, R. M., Friswell, M. I., and Inman, D. J., A Review of Morphing Aircraft, *Journal of Intelligent Material Systems and Structures*, Vol. 22, No. 9, pp. 823–877, 2011. doi:10.1177/1045389X11414084.

[2] De Gaspari, A., Ricci, S., Antunes, A., Odaguil, F., and Lima, G., Chapter 6: Expected Performances, *Morphing Wing Technologies – Large Commercial Aircraft and Civil Helicopters*, Butterworth–Heinemann, pp. 175 – 203, 2018. doi:10.1016/B978-0-08-100964-2.00006-X.

[3] Kan, Z., Li, D., Zhao, S., Xiang, J., and Sha, E., Aeroacoustic and aerodynamic characteristics of a morphing airfoil, *Aircraft Engineering and Aerospace Technology*, Vol. 93, No. 5, pp. 888 – 899, 2021. doi:10.1108/AEAT-11-2020-0263.

[4] Vasista, S., Nolte, F., Monner, H. P., Horst, P., and Burnazzi, M., Three–dimensional design of a large-displacement morphing wing droop nose device, *Journal of Intelligent Material Systems and Structures*, Vol. 29, No. 16, pp. 3222–3241, 2018. doi:10.1177/1045389X18770863.

[5] Vasista, S., Tong, L., and Wong, K. C., Realization of Morphing Wings: A Multidisciplinary Challenge, *Journal of Aircraft*, Vol. 49, No. 1, pp. 11 – 28, 2012. doi:10.2514/1.C031060.

[6] Barbarino, S., Pecora, R., Lecce, L. V., Concilio, A., Ameduri, S., and Rosa, L. D., Airfoil Structural Morphing Based on S.M.A. Actuator Series: Numerical and Experimental Studies, *Journal of Intelligent Material Systems and Structures*, Vol. 22, pp. 1004 – 987, 2011.

[7] De Gaspari, A. and Ricci, S., Application of the Active Camber Morphing Concept Based on Compliant Structures to a Regional Aircraft, *Industrial and Commercial Applications of Smart Structures Technologies (SPIE 2014)*, Vol. 9059, SPIE, K. M. Farinholt, S. F. Griffin (Eds.), San Diego, CA, USA, pp. 1 – 21, 9 March 2014. doi:10.1117/12.2045225.

[8] De Gaspari, A., Riccobene, L., and Ricci, S., Design, Manufacturing and Wind Tunnel Validation of a Morphing Compliant Wing, *Journal of Aircraft*, Vol. 55, No. 6, pp. 2313–2326, 2018. doi:10.2514/1.C034860.

[9] De Gaspari, A., Multiobjective Optimization for the Aero-Structural Design of Adaptive Compliant Wing Devices, *Applied Sciences*, Vol. 10, No. 18, pp. 30, 2020. doi:10.3390/app10186380.

[10] Kulfan, B. M., Universal parametric geometry representation method, *Journal of Aircraft*, Vol. 45, No. 1, pp. 142–158, 2008.

[11] Wang, C., Khodaparast, H. H., Friswell, M. I., Shaw, A. D., Xia, Y., and Walters, P., Development of a morphing wingtip based on compliant structures, *Journal of Intelligent Material Systems and Structures*, Vol. 29, No. 16, pp. 3293–3304, 2018. doi:10.1177/1045389X18783076.

[12] De Gaspari, A., Cavalieri, V., and Ricci, S., Advanced Design of a Full-Scale Active Morphing Droop Nose, *International Journal of Aerospace Engineering*, Vol. 2020, pp. 1–19, 2020. doi:10.1155/2020/1086518.